Comptes Rendus

Physique

Antoine Strugarek

Interactions of exoplanets with their environment

Part of Special Issue: Exoplanets

Exoplanets / *Exoplanètes*

Interactions of exoplanets with their environment

Interactions des exoplanètes avec leur environnement

Antoine Strugarek[a]

[a] Université Paris-Saclay, Université Paris Cité, CEA, CNRS, AIM, 91191, Gif-sur-Yvette, France

E-mail: antoine.strugarek@cea.fr (A. Strugarek)

Abstract. Exoplanets on close-in orbit are subject to intense interactions with their host star. They receive a strong irradiation from the star, trigger tides within their host, and stars and close-in planets can be magnetically connected. In this review, I introduce the physical concepts behind these three types of interaction. I provide simple scaling-laws for their relative strengths, and highlight the aspects of the interactions that still elude our understanding. For each interaction, I also review their detectable effects on both specific star-planet systems and on the population of exoplanets as we know it today.

Résumé. Les exoplanètes en orbite rapprochée sont soumises à des interactions intenses avec leur étoile hôte. Elles reçoivent une forte irradiation de l'étoile, déclenchent des phénomènes de marées dans leur hôte, et les étoiles et les planètes proches peuvent être connectées magnétiquement. Dans cette revue, je présente les concepts physiques qui sous-tendent ces trois types d'interaction. Je présente des lois d'échelle simples pour estimer leurs forces relatives et je souligne les aspects des interactions qui échappent encore à notre compréhension. Pour chaque interaction, je passe également en revue leurs effets détectables à la fois sur des systèmes étoile-planète spécifiques et sur la population d'exoplanètes telle que nous la connaissons aujourd'hui.

1. Introduction: the population of hot exoplanets and the solar system planets

Following the discovery of 51 Peg b [1], more than 5000 exoplanets have been detected so far. The observed population of exoplanets presents a wide variety of masses, radii, compositions; but also a wide variety of orbital properties. In particular, a wealth of planets orbiting very close to their star has been unveiled, with orbital periods often shorter than ten days. These planets are the easiest to detect and therefore occupy a large part of the sample of detected exoplanets. Nevertheless, they are not necessarily the most representative of the population of planets in our galaxy [2]. The detection techniques of exoplanets will be presented in other reviews of this special issue [3, 4]. Here, we focus on a few specificities of the population of exoplanets as we know it today, in comparison to the solar system planets.

The planets in orbit close to their stars are subject to different interactions with their environment, which we illustrate in the three panels of Figure 1. Note that in all panels, the horizontal axis represents the distance of the planet from the star which increases from left to right.
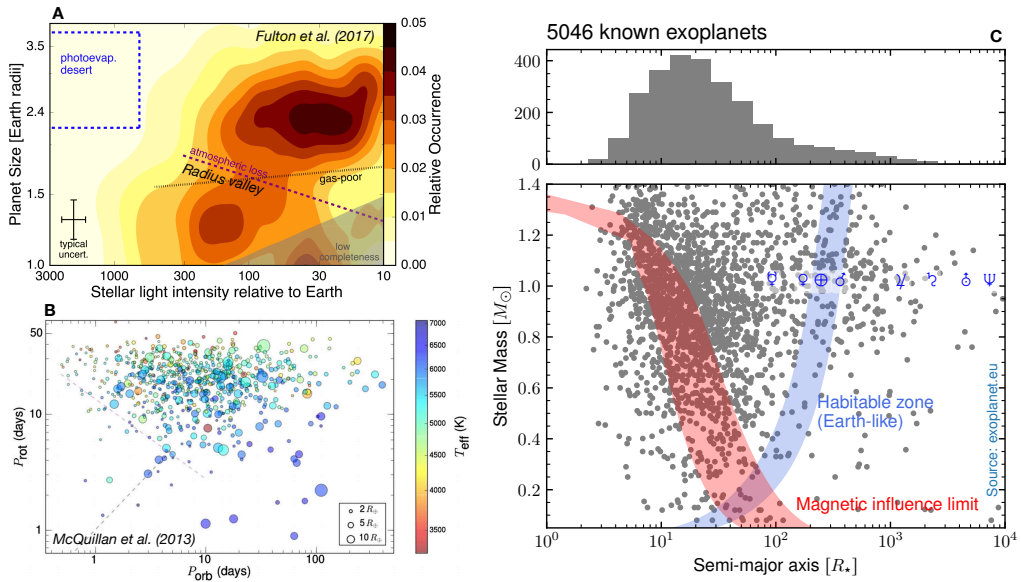
Figure 1. A. Photo-evaporation desert and radius valley, adapted from [5]. The occurrence of planet is shown as a function of the planet size (vertical axis) and stellar irradiation (horizontal axis), based on the exoplanet population known in 2017. **B.** Kepler Objects of Interest with detected candidate exoplanet (the horizontal axis corresponds to the planet orbital period) and detected stellar rotation period (vertical axis). The symbol size is scaled with the radius of the planet candidate, and the color labels the effective temperature of the host star. Adapted from [6]. **C.** Distribution of exoplanets from the exoplanet.eu database (as of May 25th, 2022), shown as a function of the mass of the host star (vertical axis) and the semi-major axis of the planet in units of the stellar radius (horizontal axis). The habitable zone for an Earth-like planet is shown by the blue area [7]. The solar system planets are labelled with blue symbols. The red area corresponds to an estimate of the magnetic influence area of the host star, which corresponds to the stellar wind Alfvén surface (see § 4).

First, we note that planets on close-in orbits can receive a large irradiation flux from their host star due to their proximity. This can lead to evaporation of their atmosphere, and it is illustrated in panel A which shows the relative occurrence of planets as a function of their mass (vertical axis, here zoomed close to the Earth mass range) and irradiation level (horizontal axis). The planet distribution is depleted slightly above the Earth mass regime, which is known as the hot Neptune of photo-evaporation desert [8] (top left corner, which exists only for strong irradiation). Above this desert (not shown here), the population of planets rises again, with many Jupiter-like planets (dubbed hot Jupiters). In panel A, another remarkable feature is seen in the distribution of radii which is known as the *radius valley* [5]: a gap in the population of Earth-like planet around $1.8\,M_\oplus$. This gap is thought to originate from atmospheric losses due to evaporation (see §2). It weakens with orbital distance and depends on the mass of the host star [9].

Second, the proximity of hot planets to their host increases the strength of their tidal interactions. This effect is illustrated in panel B, where the Kepler Object of Interests are shown as a function of the host star orbital period (vertical axis), the orbital period (horizontal axis), and colored with the effective temperature of the host star [6]. A dearth of hot planets (i.e. on short orbits) can be identified around fast rotators (lower left part of the figure). This dearth can be attributed to strong tidal (§ 3) and magnetic (§ 4) interactions.

Third, planets on close-in orbit bath in an interplanetary medium that can be dense and strongly magnetized, which leads to strong magnetic interactions. This is illustrated in panel C, where the heterogeneous population of detected exoplanets is shown in as a function of the hosting star mass (vertical axis) and the orbital semi-major axis (horizontal axis), in units of stellar radius. The top panel presents the aggregated histogram of the known exoplanets as a function of their semi-major axis, which is heavily biased towards planets on compact orbits with a semi-major axis typically smaller than 20 stellar radii. The solar system planets are shown by their symbol in blue. On this panel, we have also added the magnetic interaction limit (red area) which is estimated with a simple stellar wind model taking into account uncertainties on the rotational period of the host star. If a planet is in orbit below this interaction limit, it means it orbits in a stellar wind which is sub-alfvénic and a direct magnetic connection between the star and the planet can occur (see § 4). We observe that a large fraction of the known exoplanet population is within or close to this limit. For the sake of completeness, we have also added on panel C an estimate of the Earth-like habitable zone in blue [7].

Following this quick *tour d'horizon*, we will give a general overview of each of the three interactions in § 2, § 3, and § 4. In each case, we lay out the basic physical concepts of the interaction, provide the references to the most recent efforts devoted to their understanding, and detail the existing observational evidences for them. We conclude and provide some perspectives on the expected future directions for these fascinating research topics.

2. Radiative and wind-atmosphere interactions

2.1. *Physical concepts*

Close-in planets orbits in a dense medium compared to the Earth, and are subject to strong irradiation from their host star. Several processes can lead to the escape of material from the atmosphere of planets to the interplanetary medium. Multiple reviews have already covered most of the processes thought to be at stake, and we defer the reader to [10] for a review focused on Mars, and to [11, 12] for reviews focused on both solar system bodies and exoplanets. Let us here simply recall the broad categories of escape, not distinguishing specifically the cases of telluric or gaseous planets for the time being. Escape processes can be categorized into two regimes: thermal escape and non-thermal escape. The former originates from the bulk temperature of the

atmosphere of the planet leading to its escape, while the latter refers to an escape triggered by particle-particle and plasma interactions.

Thermal escape can be further categorized into two families: Jeans escape, and hydrodynamical escape. Jeans escape corresponds to the situation where particles in a thermal bath exceed the escape speed of the planet $v_{esc} = \sqrt{2GM_P/r_{eb}}$. This escaping process can happen if one assumes that the mean-free path of a particle overcomes the local scale height of the thermal bath, i.e. that the medium becomes essentially collisionless. This happens at the so-called *exobase*, here denoted r_{eb}. Conversely, the hydrodynamic escape corresponds to the situation where the bulk temperature of the atmosphere is large enough such that the pressure gradient between the atmosphere and the interplanetary medium drives a hydrodynamic escaping wind. This situation is akin to the well-known solar (and stellar) wind, as first theorized by Parker in 1958 [13]. In both cases, the temperature in the atmosphere needs to exceed a threshold to allow for the escape. The main driver maintaining such temperatures is the incoming extreme UV (EUV) and X-ray fluxes from the host star, denoted here F_{EUV}. This radiation is composed of photons with wavelengths shorter than 912 Å (the ionization threshold of hydrogen) which ionize the hydrogen of the planetary atmosphere and deposit heat during this process (e.g. [14]). The bulk heating comes from photons close to this threshold, because the cross-section of the bound-free absorption of hydrogen varies with the cube of the wavelength. The transition between the Jeans and hydrodynamic escape is determined by the Jeans parameter [12]

$$\lambda_{ex} = \frac{GM_P m_{el}}{r k_b T} = \frac{v_{esc}^2}{v_{el}^2}, \tag{1}$$

where m_{el} and v_{el} and respectively the mass and the thermal speed of the escaping chemical component el, T the temperature of the atmosphere, and k_b the Boltzmann constant. If λ_{ex} is small, Jeans escape naturally occurs. If it is large, the hydrodynamic escape prevails. The exact value of the transition depends on the composition of the atmosphere (e.g. [15, 16]). In the case of hydrodynamic escape, several prescription have been proposed in the literature. Based on an energy-limited approach, [17] derived a mass-loss rate formulation based on the equilibrium between the heat deposition of the incoming stellar extreme UV flux and the gravitational potential of the planet. In this case, one can derive the following formula

$$\dot{M}_P \sim \frac{\alpha F_{EUV} \pi R_P^2}{GM_P/R_P} \sim 1.4 \times 10^7 \alpha \left(\frac{R_P}{10^8 \, m}\right)\left(\frac{M_J}{M_P}\right)\left(\frac{F_{EUV}}{0.45 \, W \, m^{-2}}\right) \, kg \, s^{-1}, \tag{2}$$

where α is a factor between 0 and 1 quantifying the fraction of the heat received from the star that is put to work against gravity. If F_{EUV} is large, the radiative cooling (proportional to n^2) in the planetary atmosphere starts to participate to the balance. This gives $n \propto F_{EUV}^{1/2}$ and the mass loss rate scaling-law becomes

$$\dot{M}_P \sim 4 \times 10^9 \left(\frac{F_{EUV}}{500 \, W \, m^{-2}}\right) \, kg \, s^{-1}. \tag{3}$$

These scaling laws provide a useful first-order estimate of the atmospheric mass-loss, but can predict mass losses varying from one or two orders of magnitude depending which scaling law is used. They are furthermore generally applicable only to pure-hydrogen atmospheres. They predict maximum evaporation rates of about $10^9 - 10^{10}$ kg/s for the hottest and most massive planets we know, which is a good upper limit as of today on the atmospheric escape rate. This can lead to fast atmosphere erosion for low-mass planets: the atmosphere of the Earth has a mass of about 5×10^{18} kg which would be lost in about 16 years under such extreme escaping conditions! These scaling laws nevertheless neglect many aspects of the real, three-dimensional geometry and day-night asymmetry of the escaping atmosphere, as well as more complex non-thermal escape processes.

Non-thermal escape can take a variety of form, depending on the planet (its mass and composition), and on its host star. It is driven either by the irradiating flux from the host star, or by the interaction of the upper atmosphere with the stellar wind. The photons from the star can lead to photochemistry in the upper atmosphere in the form of, e.g. ion recombination or photo-dissociation of molecules. Both reactions can be exothermic, and therefore ultimately contribute to the escape of atmospheric components. Conversely, the exposure to the stellar wind can lead to charge exchange between the ionized wind and the neutral atmosphere, to the induction of ionospheric outflows, or to the mixing and escape of components by hydrodynamic and/or plasma instabilities at the interface between the two media. These processes can depend on the existence or non-existence of a magnetosphere or of an ionosphere, which existence can be questioned depending on the level of irradiation. Some lead to the escape of components in an ionized form, while other lead to the escape of neutral elements, often dubbed energetic-neutral-atoms (ENA). This distinction is of paramount importance for the detection and understanding of escaping atmospheres, as most of the detectable signal from such object is tied to the distribution of neutrals in the environment of exoplanets. We will not detail these mechanisms here for the sake of brevity, and defer again the reader to the review of [12] for a complete description. We note though that in the solar system, for instance, photochemistry dominates atmospheric escape at Mars, while at Venus ionospheric escape is thought to be the leading mechanism [11]. When considering hot exoplanets, caution is therefore in order when assessing which process dominates.

In the context of massive planets on close-in orbits, the irradiation of their upper atmosphere can lead to a variety of phenomena. Due to their strong gravitational potential, the stellar irradiation can lead to the inflation of their atmosphere while keeping most of it gravitationally bound. Nevertheless, ultra-hot Jupiters still intercept a very energetic stellar EUV flux and can therefore reach an escaping atmosphere state. In this context, the morphology of the escape can be of different types. Based on numerical simulations where the thermal escape rate of the planetary atmosphere is prescribed *a priroi*, [18] have classified escape patterns into four broad families. These families are illustrated in Figure 2 and can be classified depending on the ratios between three characteristic length scales.

The first length scale is the Hill radius

$$R_t = \left(\frac{M_P}{3M_\star}\right) R_{\mathrm{orb}},$$

(4)

which corresponds to the L1 Lagrange point of the orbital system. It characterizes how much the escaping flow is influenced by the gravitational potential of the star.

The second length scale is the distance at which the ram pressure of the escaping planetary wind matches the ambient pressure of the stellar wind P_{amb}. The latter is the sum of three contributions: the thermal pressure of the stellar wind, its magnetic pressure, and the ram pressure in the frame where the planet is at rest. The stand-off distance is defined as pressure equilibrium distance such that

$$R_w = \left(\frac{\dot{M}_P v_{w,p}}{4\pi P_{\mathrm{amb}}}\right)^{1/2},$$

(5)

where $v_{w,p}$ is the speed of the planetary wind at R_w.

Finally, a third length scale can be defined when the planet possesses its own magnetic field and an associated magnetosphere. In that case, the pressure equilibrium can be reached between the ambient pressure P_{amb} and the magnetic pressure of the planetary magnetosphere. Assuming

a dipole field for the magnetosphere and a surface magnetic field B_P at $r = R_P$, the magnetic stand-off distance can be approximated by

$$R_m = R_P \left(\frac{B_P^2}{2\mu_0 P_{\text{amb}}} \right)^{1/6} , \quad (6)$$

where we have assumed S.I. units and μ_0 is the permeability of free space.

The morphology of the escaping atmosphere can then be characterized as follows ([18], see Figure 2):

- $R_t > R_m > R_w$ (Type I): In this case, the planetary outflow is weak, and the stellar wind is intercepted by the planetary magnetosphere ($R_m > R_w$, top left panel). The tail angle depends on the incoming stellar wind orientation, and the tail width is directly controlled by the size of the planetary magnetosphere.
- $R_t > R_w > R_m$ (Type II): In this case, the planetary outflow is strong and the stellar and planetary wind directly collide ($R_w > R_m$, top right panel). A bow shock is formed at the interface. An accumulation of the escaping material can occur at its apex, which could be at the origin of some detections if it remains sufficiently neutral (see § 2.2).
- $R_w > R_m$ and $R_w > R_t$ (Type III): The type III interaction is a stronger version of the type II interaction, whereby the planetary wind is so strong (or the gravity of the planet is not strong enough, $R_w > R_t$, bottom left panel) that only part of the escaping material is swept back into a tail, while the other part falls down towards the host star.
- $R_m > R_w$ and $R_m > R_t$ (Type IV): The type IV interaction corresponds also to a case where the interaction takes place out of the Hill radius of the planet, but in this case the planetary outflow is weaker ($R_m > R_w$, bottom right panel). This case is comparable to a classical Roche lobe overflow process, except that the magnetized stellar wind also plays an important role in shaping the escape route for the atmospheric material.

The four types of interaction could in principle occur in close-in star-planet systems. The control parameters of the interaction are the spectral type of the host star, the orbital distance of the planet, and the mass and the composition of the planet. The star controls the characteristics of the wind, which determines the ambient pressure surrounding the planet and participates in non-thermal escaping processes (see above). It also provides the main energy source powering the atmospheric escape by its EUV and X-rays fluxes. We note that in this work and in this classification, the outflow is assumed to be fully ionized. This is not necessarily the case in reality, especially on the night side of the planet. This leads us to discuss the limitations of the above simple physical ingredients we have introduced, and the modelling efforts that are being carried out to overcome these limitations.

The first limitation comes from the real geometry of star-planet systems. The planets can have a complex orbit and therefore be subject to a wind and radiative environment that varies on a timescale of a few days or even less. In addition, the interaction is fundamentally 3D due to the orbital direction and the star-planet axis which differ. The magnetic field of the planet can also have an angle with respect to these axes. These aspects require the use of numerical models to quantify adequately the mass loss rate of exoplanets, and the shape any visible feature associated with the escaping atmosphere in and out of transit [19, 20]. The second limitation of the simplified approach we laid out naturally comes from the complexity of the photochemical network of reactions that depends on the composition of the planetary atmosphere as well as the EUV and X-rays spectrum of the host star. In this context, again, numerical simulations are required to compute in an *ab-initio* manner the photochemical reactions and the associated continuity equations for the various species as well as the heat exchanges associated with these reactions [21]. Finally, an often overlooked aspect of such interaction lies in the stellar variability. Active stars produce strong flares and energetic particles that can play a role in the escaping
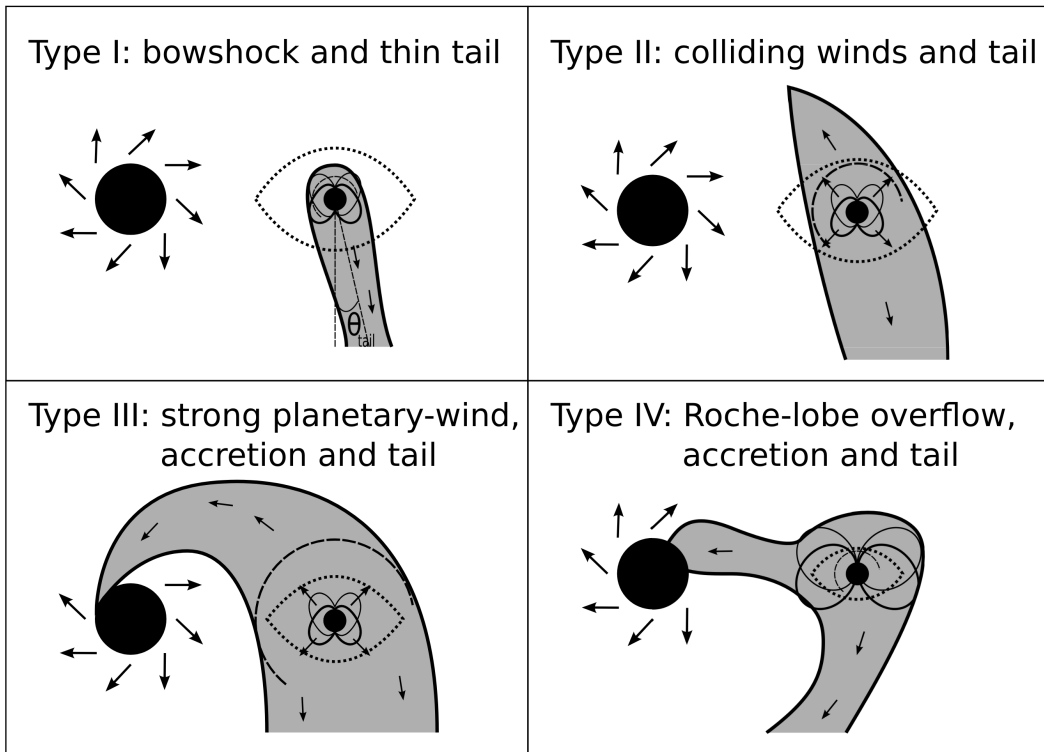
Figure 2. Types of planetary escape flows under strong irradiation (adapted from [18]), viewed on top of the orbital plane in the frame where the planet is at rest. Four types of outflow have been identified (see text). The dotted line corresponds in each panel to the effective gravitational potential and passes through the Lagrange point L1 on the planet-star line. The dashed arcs in panels II and III correspond to the distance at which the ambient pressure of the stellar wind is in equilibrium with the ram pressure of the planetary wind. The grey areas delimited by solid lines represent the escape patterns.

processes of planetary atmospheres [22]. Therefore, they should be considered when assessing the atmospheric state of hot planets around active stars.

2.2. *Observable effects of radiative and wind-atmosphere interactions*

After a quick review of the physical ingredients behind the radiative and wind-atmosphere interactions for hot exoplanets, let us discuss the available observational evidence for these processes.

The first detection of an escaping atmosphere has been provided by [23]. They detected an absorption in Lyman-α of HD 209458 during three transits of HD 209458b with the Hubble Space Telescope, and showed it corresponded to a location beyond the Roche lobe of the planet, and therefore could be interpreted as planet evaporation. This detection is illustrated in Figure 3. Since then, multiple detections of such evaporating atmospheres have been reported for famous systems such as HD 189733, WASP-12, or GJ 436. We defer the reader to the recent review [24] on that topic. We can hope that future space-based UV observatories, such as LUVOIR would give access to more targets and constraints for our understanding of evaporating atmospheres.
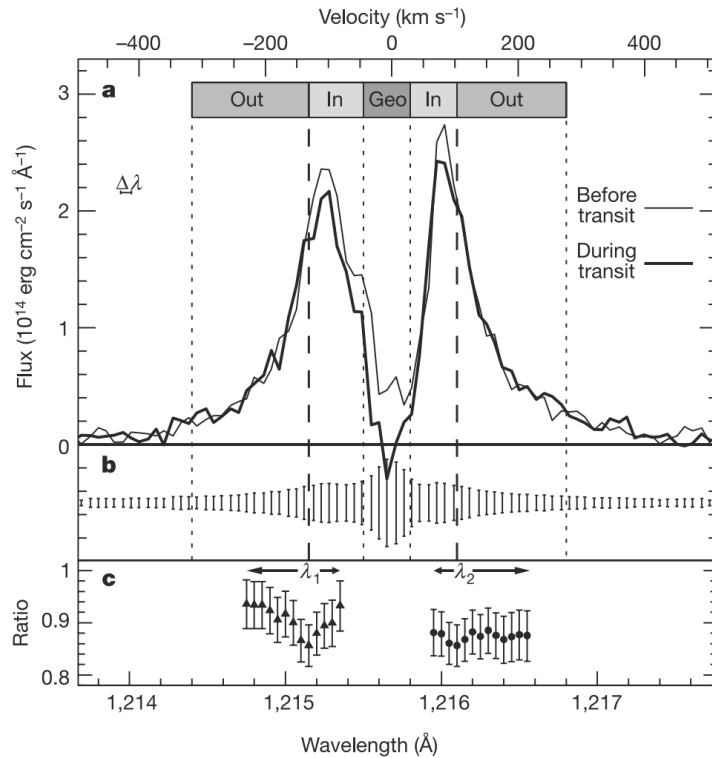
Figure 3. First detection of an absorption in Lyman-α that originates from an outflowing atmosphere, as originally published in [23]. The top panel (a) shows the Lyman-α profile, during transit (thick line) and before transit (thin line). A clear absorption can be seen in the blue wing on the left (labeled 'In'), with a flux lesser by about 10% to 15% during transit. The lower panel (c) shows the ratio between the two spectra in the two wings. In this panel, the central part of the spectrum was not considered as it is polluted by geocoronal emission ('Geo' domain). The middle panel (b) shows the errors bar for each spectra bin. More details can be found in [23].

Furthermore, optical and near-infrared instruments can also provide constraints on other upper atmosphere tracers, such as sodium in the atmosphere of low-mass planets.

Indirect tracers of escaping atmospheres have also been proposed in the literature. In the context of type III evaporation (see § 2.1), the atmospheric material falling onto the host star could create hot spots or at least features in the stellar spectrum. This was first proposed for instance as an explanation for an anomaly in the CaII K line of HD 179949 and τ-Boo [25], or for the excess of X-rays and far-UV emission of HD 189773 [26]. This interpretation must be taken with caution, though, as the significant phase shift between the planet position and the phase of these features on the stellar disk is large and cannot be as easily explained by material falling from the hot Jupiter. In addition [27] found an opposite situation for WASP-12 that exhibits anomalously low chromospheric emissions. Such dimming was also reported for WASP-18, and could be due to absorption by circumstellar material originating from its close-in outgasing planet [28].

Other striking evidences of planet evaporation are found in the demographics of hot exo-planet, as illustrated on panel A in Figure 1. First, the hot sub-Jovian desert (dearth of planets in the top left corner of the panel with masses lower than 0.5-0.7 M_J on orbital periods lower than about 3 days) is probably at least in part due to photo-evaporation. Indeed, planets with $M_P \lesssim 0.2 M_J$ have likely too weak gravitational force to hold their external layer under strong insulation from their host. They lose a portion of their mass and subsequently fall into a category of lower-mass planets, creating part of the sub-Jovian desert. The origin of the higher end of the desert (not shown in Figure 1) is more uncertain as of today, but could originate from e.g. high-eccentricity migration [29]. In addition, the radius valley in the distribution of small planets [5] is likely also due to evaporating atmospheres. [30] presented a simple and convincing model based on an energy-limited approach (see § 2.1) which reproduces a radius valley for low mass planets on orbit shorter than about 20 days. More precise computation of photo-evaporation rates for such planets should consider all other mechanisms we laid out in the preceding sections, and some efforts in that direction are currently underway in the community (*e.g.* [31, 32]).

3. Tidal interactions

3.1. *Physical concepts*

Tidal interactions consist in the gravitational response of a non-punctual body A to another body B. Such perturbations induced by body B can be dissipated in rocky or fluid layers of body A, which in turn affects the dynamics of the body B. In the context of star-planet systems, tidal forces can affect the rotation of each body and their respective orbist. They can change the eccentricity and the inclination of the smaller body's orbit, and can also lead to atmosphere-core decoupling in planets. Multiple excellent reviews are already available on tides in stars and planets (e.g. [33, 34]). We here briefly review the physical processes at stake and defer the reader to these other works for more mathematical and physical details on tides.

The gravitational perturbation applies a force $\mathbf{F}_{\text{tide}}$ on body A deriving from a tidal potential of punctual body B such that

$$\mathbf{F}_{\text{tide}}(\mathbf{r}) = \nabla \left[\frac{GM_B}{d^3} \mathrm{P}_2 (x_{\mathbf{r}}) \right], \tag{7}$$

where M_B is the mass of body B, $\mathbf{d}$ the distance vector between the centers of the bodies and $\mathbf{r}$ the position within body A on which the tidal force applies. P_2 is the Legendre polynomial of order 2, and $x_{\mathbf{r}} = \cos(\mathbf{d} \cdot \mathbf{r})$. The deformation associated with the tidal force (Eq. (7)) induces a large-scale flow in fluid layers of boday A and elastic displacement in rocky layers of body A. This phenomenon is often referred to as the *equilibrium tide* [35]. It is illustrated in Figure 4, where the adiabatic adjustment of the equilibrium tide is shown by the green ellipse (the so-called *tidal bulge*). Because body A rotates at a rate Ω_A that differs from the orbital frequency n_B ($n_B = \sqrt{GM_A/d^3}$ for a circular orbit), the bulge is out of phase. It can be in advance or delayed compared to the orbital phase if the rotation rate of body A is faster or slower than the orbital frequency. In Figure 4, we illustrate the case $\Omega_A > n_B$. The existence of a phase of the tidal bulge (denoted with an angle δ) leads to the dissipation of the bulge itself by friction. It must be nevertheless noted right away that the tidal force can also excite waves within body A. These waves are triggered at the tidal frequency $\sigma = l n_B - m \Omega_A$, with l and m spherical harmonics degrees corresponding to the complexity of the orbit. Depending on the physical conditions within body A, the tidal forcing can excite waves that can be sustained by Coriolis forces if body A is in rotation, buoyancy in stably-stratified layers, compressibility, elasticity, or even Lorentz forces in presence of a magnetic field within a conducting layer. This wave-like tide is often refereed to as a *dynamical tide*. The restoring force constrains the range of frequencies at which
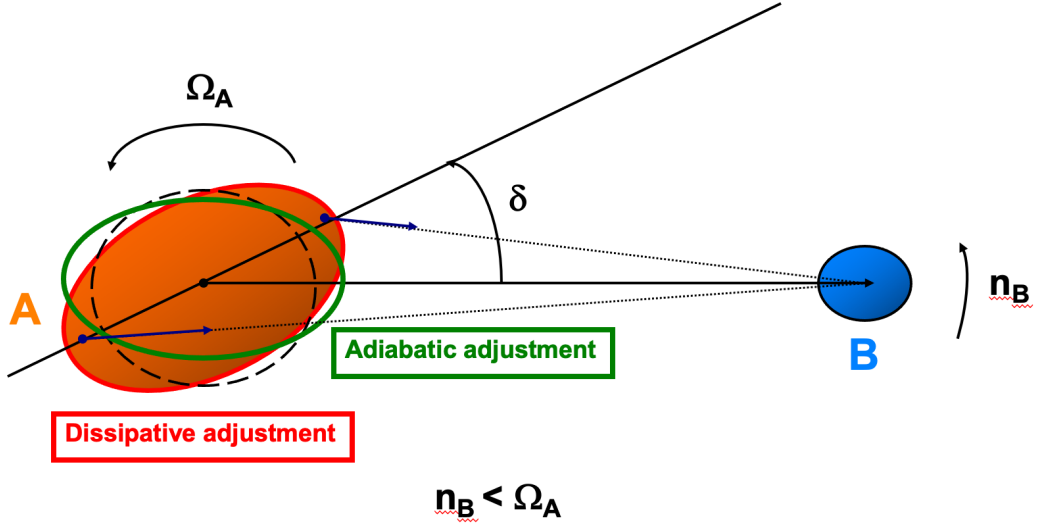
Figure 4. Schematic of the equilibrium tide, adapted from [34]. The case $n_B < \Omega_A$ is illustrated, where the tidal bulge is in advance of phase compared to the perturbator position (B). The adiabatic adjustment is shown by the green ellipse, and the net adjustment which is determined by the difference $\Omega_A - n_B$ and the dissipation properties of body A is shown by the red ellipse. The angle between the tidal bulge and the perturbator position is generally denoted δ.

dynamical tides can exist. For instance, in the case of the inertial dynamical tide, the restoring force is the Coriolis force which has a characteristic frequency of $2\Omega_A$. As a result, this specific dynamical tide can only occur if $n_B > 2\Omega_A$.

Both equilibrium and dynamical tidal responses in body A can be subject to dissipation. This dissipation can occur due to viscosity, heat diffusion, or non-linear wave interactions. This dissipation actually leads to a transfer of kinetic energy from the orbit of body B to the interior of body A. This is what occurs for instance between the Earth and the moon, and its leads the moon to migrate outward by about 3.8 centimeters per year [36]. The net torque applied to body A can be generalized through [37]

$$\Gamma_{\text{tides}} = -6 J_B n_B \frac{M_B}{M_A} \left(\frac{R_A}{d} \right)^5 \frac{k_2}{Q_A},\tag{8}$$

where J_B is the orbital angular momentum of body B (for a circular orbit, $J_B = M_P n_B d^2$), k_2 is the hydrostatic Love number of body A, and Q_A is the tidal dissipation quality factor of body A. Q_A encapsulates all the internal properties of body A and varies with the type of tidal flow considered. It is common to introduce the generalized quality factor $Q' = 3Q/(2k_2)$ [38], which reduces to $Q' = Q$ for a homogeneous body. The tidal dissipation quality factor Q is a convenient representation of the dissipation timescale of the tide, and Q' is a dimensionless version of this quality factor. The smallest Q' is, the strongest is the tidal dissipation. It can vary by many orders of magnitude depending on the internal properties of the dissipating body, and on the type of tides considered. As a result, when orbital changes can be measured, tidal theory by the means of the tidal quality factor can offer a probe of the internal properties of the orbiting body [39].

Disregarding the formulation of the torque for now, let us first consider a star-planet system with an initial stellar rotational angular momentum $J_\star = GM_\star R_\star^2 \Omega_\star$ and a planetary orbital

momentum J_P. A torque such as (8) transfers momentum from one reservoir to the other. We note that the orbital angular momentum J_P is proportional to $n_P^{-1/3}$ while the rotational angular momentum $J_\star$ is proportional to $\Omega_\star$. Therefore, the torque leads to a change in the orbital frequency that is stronger than the change of the stellar rotation rate. If we consider the case of a momentum transfer towards the star, this results in the fact that if $J_\star > 3J_P$, the torque leads to a change of orbital frequency that is too fast to reach co-rotation ($n_P = \Omega_\star$) and the planet spirals inward toward the central star until it reaches its Roche lobe. Conversely, if $J_\star \leq 3J_P$, the momentum difference between the two bodies is lesser and as the planet migrates inwards the rotation rate of the star changes significantly: the system evolves towards co-rotation where the angular momentum transfer halts.

To conclude the overview of the basic theories behind our understanding of tidal interactions, it is also instructive to explore the forms that k_2/Q_A can take depending on the type of tide considered. We will give the example here of the interior of a star, and defer the reader to more complete reviews of tidal interaction for the detailed description of tidal dissipation in solid and fluid layers of planets [34]. Let us first consider the equilibrium tide, which is the global circulation induced within body A by the tidal potential. Refining the initial approach of [35], [40] proposed an analytical model of the tidal dissipation such that

$$\left.\frac{k_2}{Q_\star}\right|_{\text{equilibrium}} \propto \frac{R_\star^3}{GM_\star^2}\left|\sigma_2 \int_0^{R_\star}\left(\frac{r}{R_\star}\right)^8 \rho\nu_t\mathrm{d}r\right|, \tag{9}$$

where ρ is the density within the star, $\sigma_2 = 2(n_P - \Omega_\star)$ is the *tidal frequency*, and ν_t is the turbulent viscosity that dissipates the tidal flow. Generally, the dissipation occurs due to the interaction of the tidal flow with turbulent motions that act as en effective viscosity. Therefore, the above integral is often only considered in convective zones within stars.

We finally note here that the dynamical tide can also be dissipated within stars. This case is nevertheless much more complex to treat, because of the nature of dynamical tides, and a specific formulation must be derived for each type of dynamical tide. We refere the readers to the aforementioned reviews [34, 38] if they want to dig deeper into this topic.

3.2. *Observable effects of tidal interactions*

The tidal interactions lead to an exchange of momentum between the two bodies. As a result, one can expect tides and their dissipation to be playing a key role in shaping the architecture of star-planet systems. In the previous section, we have detailed tides induced in body A by a punctual companion B. In reality, tidal forcing also applies within body B due to the existence of the primary body A. Both tides and their associated dissipation will add up and contribute to the rotational and orbital evolution of the two bodies.

The first effect we consider here is the migration of the less massive body B. Depending on the characteristics of bodies A and B, the migration timescale of a close-in exoplanet can theoretically vary from a few thousands years to tens of billion years. In this context, the detection of the orbital period variations has been attempted for the most promising known exoplanets. For instance, the transit-to-transit variations in the orbital period of WASP-12 ($P_{\text{orb}} = 1.09$ days) are compatible with a shift of about 30 ms/year as illustrated on Figure 5 [41–43].

Several studies attempted to constrain the quality factor of tidal dissipation Q' in gravitationally bound bodies [47]. For instance, the study of the orbit of natural satellites of Saturn led [39] to constrain the quality factor of Saturn to be $k_2/Q \simeq (15.9 \pm 7.4) \times 10^{-5}$. Likewise, the study of the demographics of exoplanets could theoretically provide constrains on Q' within exoplanets. Such studies were carried for instance by [48] who provided upper and lower limits for the tidal dissipation quality factor in both stars and orbiting exoplanets. In [49], a more detailed study
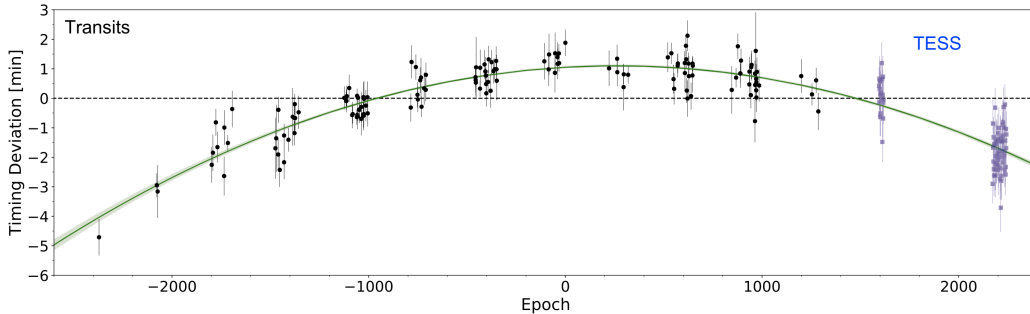
Figure 5. Orbital decay of WASP-12b, adapted from [43]. The transit data points in black were taken from [44, 45], the first TESS data points in blue from [46], and the last TESS data points from [43]. We only show here the transit data, occultation data supporting a period decay as well can be found in [43]. The horizontal axis represents the barycentric julian day centered on a specific day. The green curve corresponds to the best fit of the period decay, which is compatible with an orbit decaying by about 30ms/year (i.e. about 6 minutes / 2000 days).

on the specific population of low-mass exoplanets close to relatively massive stars was also performed. From bayesian inference, they estimate from a population of 223 systems a relatively low $Q'_\star$ lower limit ($\log Q'_\star = 8.26$), which supports the idea of an enhanced tidal dissipation due to the existence of dynamical tides [38, 50].

Finally, our understanding of tidal interactions can also benefit from the joint study of systems where the rotation of the star, its age, and the orbital period of the planets can be characterized. The excess of rotation in stars hosting hot giant exoplanets was first identified in [51]. With the Kepler mission, more targets were considered [6] and the dearth of hot exoplanet around fast rotators was cofnirmed with a sample of 737 Kepler Objects of Interest. Such a dearth is suggestive of planet engulfment due to an efficient inward migration, possibly due to tides (we note though that this evidence is still based on a relatively small sample, and revisiting this analysis is today needed, see e.g. [52]). During stellar evolution, the stellar structure changes in the pre-main sequence, and the star spins down due to magnetized winds during the main sequence. Such changes affect the tidal dissipation within the host star [53]. In some cases, the tidal dissipation is efficient enough so that hot exoplanets circularize, synchronize, and even spiral inward until engulfment [54]. It is now possible to use tidal dissipation theory to quantitatively assess this scenario [55]. It does indeed provide a good qualitative comparison with the observed population of star-planet systems, but the synthetic population produced by the most advanced models still predict a slight excess of hot exoplanets around fast rotators. This excess could originate from missing physics (such as an additional tidal dissipation mechanism, or proper inclusion of magnetic interactions, see §4), a strong bias of the initial population after disk dissipation [56], or a combination of both. In the future, the PLATO mission will provide robust estimates of the ages of such star-planet systems that will allow more precise observational constraints on the tidal dissipation quality factors, and on tidal interaction theory [57].

4. Magnetic interactions

4.1. *Physical concepts*

Planets on close-in orbits can be thought of as a perturbator within the interplanetary medium. It is subject to a drag from its environment, and can channel energy towards the central star. As a

result, the characterization of star-planet magnetic interactions requires to estimate the plasma conditions along the orbit, that are set by the stellar wind. We will not detail here stellar wind theory [13], and refer the reader to recent reviews [58, 59]. Let us summarize it as follows. Cool stars like the Sun possess an external turbulent convective envelope that is the seat of an efficient dynamo process. The associated large-scale magnetic field sculpts the environment of the star. In addition, turbulent photospheric motions are thought to excite magnetic perturbations, likely in the form of Alfvén waves, that propagate along this magnetic field and ultimately deposit their energy upper in the stellar atmosphere. Small-scale impulsive events can also participate in expelling magnetic energy into heating the stellar atmosphere. In the case of the Sun, these lead to a very hot corona, reaching more than a million Kelvin. This hot corona leads to the existence of a stellar wind, accelerating outwards and reaching supersonic and superalfvénic speeds. At the Earth orbit, the solar wind speed averages between 400 and 700 km/s, and reaches an alfvénic Mach number M_a between 9 and 10! These conditions can strongly vary in the context of hot exoplanets.
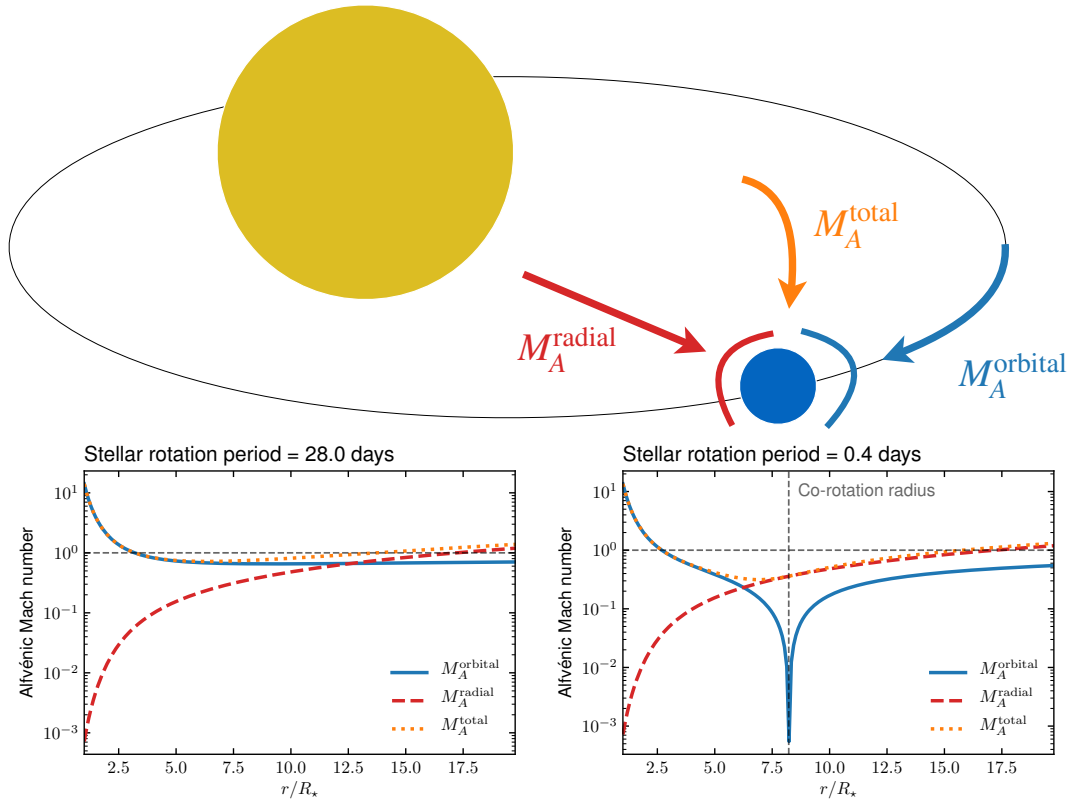

Figure 6. Schematic of alfvénic Mach numbers in compact star-planet systems. The top panel illustrates the star (yellow), the planet (blue) and its orbit (black), and the direction associated with the alfvénic Mach numbers (Eqs. (10)-(12)). The red and blue circular arcs label the position of possible shocks. The bottom panels show the values of these numbers as a function of orbital distance. The left panel corresponds to a Sun-like star, and the right panel to a young, fast-rotating Sun. Adapted from [60], and inspired from [61].

We can get a first estimate of the wind conditions at a given distance from the star by computing a simple Weber–Davis wind solution under the influence of rotation [62]. Three

alfvénic Mach numbers can be computed, each characterizing different aspects of star-planet magnetic interactions. They are illustrated in the top panel of Figure 6 and are defined as follows

$$M_A^{\text{radial}} = \frac{v_r^w}{v_A}, \tag{10}$$

$$M_A^{\text{orbital}} = \frac{\left| v_\varphi^w - v_{\text{kep}} \right|}{v_A}, \tag{11}$$

$$M_A^{\text{total}} = \frac{\left| \mathbf{v}^w - \mathbf{v}_{\text{kep}} \right|}{v_A}, \tag{12}$$

where $\mathbf{v}^w$ is the stellar wind velocity field. The Kepler velocity $\mathbf{v}_{\text{kep}}$ is assumed here to correspond to a circular orbit. Finally, $v_A = B_w/\sqrt{\mu_0 \rho_w}$ is the local Alfvén speed at the planet orbit based on the plasma properties in the stellar wind.

In the bottom panels of Figure 6 we illustrate the three alfvénic Mach numbers for a Sun-like star on the left and a fast rotating Sun (e.g. a young Sun) on the right. The classical alfvénic Mach number (Eq. (10)) is shown by the red dashed lines. For the Sun (left panel), this simplified 1D model predicts an average alfvénic point around 17 solar radii (see also the red area in panel C of Figure 1), which is relatively close to the latest estimates from Parker Solar Probe [63]. The orbital alfvénic Mach number M_A^{orbital} is shown in blue. It is super-alfvénic very close to the star, due to a very fast keplerian motion. We see that it remains nevertheless sub-aflvénic for most of the domain for a Sun-like star. In the case of an extremely fast-rotating star (right panel), the co-rotation radius (vertical dashed line) can be in the sub-alfvénic domain of the stellar wind. At the co-rotation radius $M_A^{\text{orbital}} = 0$ by definition, which means that the magnetic interaction vanishes in the direction of the orbit. Finally, the total Alfvénic Mach number (Eq. (12)) is shown by the orange dotted line, and matches the maximum of the two other Mach numbers. Following this basic analysis, we can conclude that most planets orbiting below 10 to 20 $R_\star$ are likely to be in a sub-alfvénic interaction regime [64] (see Figure 1, panel C). Such planets are therefore likely to be magnetically connected to their host star. We now turn to the basic description of different magnetic connection scenarii in this sub-alfvénic regime.

The perturbations that a planet triggers in the interplanetary medium can be decomposed as magneto-hydrodynamic (MHD) waves traveling away from the planet location. In the family of MHD waves, pure Alfvén waves are degenerate (their group velocity is equal to the Alfvén speed and does not depend on the wave vector) and therefore they carry most of the energy involved in the interaction in a focused manner away from the perturbator [65]. A net Poynting flux is thus channeled away from the planet by the Alfvén waves, along what is often referred to as Alfvén wings. If the perturbator lies in a sub-alfvénic region of the stellar wind, the alfvénic perturbations can travel back and forth between the star and the planet due to reflections induced by Alfvén speed variations in the stellar wind and in the low atmosphere of the star. In the context of star-planet systems, a simple estimate of the ratio between the alfvénic travel time and the advective timescale of the flow across the obstacle can be found in [66]. In essence, what is found is that for obstacles constituted by a planet and its magnetosphere, alfvénic perturbations generally do not have time to perform a back and forth travel between the planet and the low atmosphere of the star during the advective crossing timescale. This situation corresponds to the so-called *pure Alfvén wing case* [65] and is often referred to as a *dipolar interaction*. Other scenarios can be achieved, depending on the propagation time of these waves and on the conductive properties of the planet (in the context of Jupiter and its moons, see [67, 68]). For instance, [69] showed that planets with no magnetosphere and high internal conductivities could lead to the opposite situation, where Alfvénic perturbations have time to perform multiple back-and-forth travels. The latter case is generally referred to as the *unipolar inductor* interaction regime. In

this interpretation, it is common to use an analogy with an electric circuit. The planet drives an electromotive force, and the electric circuit is composed of the planet, the wing in between the planet and the star, and the atmosphere of the star where Alfvén waves bounce back. Each part can be associated to an equivalent resistance $\mathscr{R}$ [69]. In most unipolar inductor models, the dominant resistance is considered to be the one of the stellar atmosphere. In that situation, the unipolar inductor model leads to very strong magnetic interactions. Nevertheless, this situation is not necessarily always achieved. First, [70] argued that if the total resistance of the circuit (in Ohms) is such that

$$\mathscr{R}_{\text{tot}} < \mathscr{R}_{\text{crit}} = \frac{4\mu_0}{\pi} a \left| \frac{2\pi}{P_{\text{orb}}} - \Omega_\star \right|, \tag{13}$$

where a is the semi-major axis, then the expected toroidal field is so intense that the wing should break and reconnect by means of kink-like instabilities. This scenario, sometimes referred to as the *stretch-and-break* mechanism, was also studied in depth in [71]. It is important to note that $\mathscr{R}_{\text{crit}} \simeq 0.1$ Ohms for a planet on a 10 days orbit around a solar twin, while $\mathscr{R}_\star \simeq 10^{-5}$ Ohms according to [69]. Therefore, this significantly lessens the strength of the unipolar interaction as modelled by [69] due to a much higher effective resistence. Second, the mere propagation of Alfvén waves within the stellar corona is also limited by the Alfvén conductance $\Sigma_A = (\mu_0 v_A)^{-1}(1 + M_A^2 - 2M_A \sin\Theta)^{-1/2}$ (where Θ is the angle between the relative orbital velocity and the perpendicular to the ambient magnetic field), as shown by [72]. The equivalent Alfvén resistance $R_A = 1/\Sigma_A$ ranges typically between 0.02 and 3 Ohms for a planet on a 10 days orbit around a solar twin, and can therefore also be a limiting resistance for the electric circuit as well. These two limitations severely weaken the magnetic interaction envisioned by [69] for their unipolar inductor, which can in the end be understood as a prolongation of the dipolar interaction case (see also [68]).

The energy channeled by the interaction towards the star can be estimated by the Poynting flux carried by Alfvén waves through [74]

$$\mathscr{P} = \int_{AW} \mathbf{S} \cdot d\mathbf{A} \simeq 2\pi R^2 \bar{\alpha}^2 \left(1 + M_A^2 - 2M_A \sin\Theta\right)^{1/2} S_{AW}, \tag{14}$$

where R is the effective radius of the obstacle, and $\bar{\alpha} = \Sigma_P/(\Sigma_P + \Sigma_A)$ quantifies the conductive properties of the obstacle (where Σ_P is the Pedersen conductance in the planet's ionosphere). These results were later confirmed and extended to more complex geometries through 3D numerical simulations [75, 76]. The maximal power is obtained for high conductance in planet's atmospheres, for which $\bar{\alpha} = 1$. In the solar system, $\bar{\alpha}$ varies from a few 10^{-2} to about 1 for the different moons of Jupiter and Saturn [74, 77]. The conductive properties of exoplanets are nevertheless largely unknown as of today. They depend for instance on the complex photochemical reactions in their upper atmosphere, and hence on both the irradiation received by the planet, and the planet atmospheric composition (see § 2). Both are expected to change significantly along stellar evolution. Ab-initio calculations are today being performed to characterize (among other aspects) the conductive properties of exoplanets' atmosphere (e.g. see the Kompot code [78]).

The magnetic torque felt by close-in exoplanets can also be expressed in a simplified form with was also. A simplified version of this scaling law can be written as

$$\Gamma_{\text{mag}} = C_{\text{drag}} (M_a, \Theta_M, B_P) A_{\text{obst}} P_t, \tag{15}$$

where P_t is the total pressure of the medium in which the planet orbit, A_{obst} is the obstacle area offered by the planet and its magnetosphere, and C_{drag} is a drag coefficient that depends on the alfvénic Mach number, the angle Θ_M between the planetary field and the ambient field and the planetary field strength B_P. This torque was systematically parameterized through numerical simulations [75, 76] and can lead to a migration timescale as short as a few million years when planets are in close-in orbit around young active stars [79]. Magnetic interactions can therefore
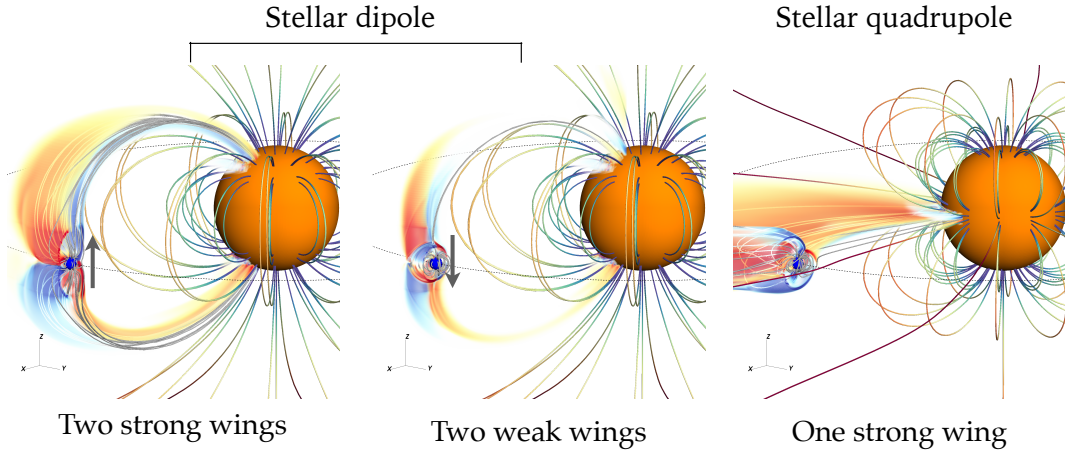
Stellar dipole   Stellar quadrupole

Two strong wings   Two weak wings   One strong wing

Figure 7. Topology of Alfvén wings deduced from numerical simulations [73]. In each panel, the wings are materialized by a volume rendering of positive/negative currents in red/blue. The magnetic field lines of the stellar wind and corona are shown by the colored tubes. The two left panels show the example of two wings connecting the star and the planet. In the second panel, only the orientation of the planetary field has been reversed, showing no change in the connectivity path of the wings but affecting strongly the strength of the magnetic interaction. On the right panel, the topology of the stellar magnetic field is quadrupolar and in this case only one wing connects the planet to the star. The other wing still exists, but extends away from the star into the interplanetary medium. Adapted from [73].

sometimes add up to tidal interactions and affect the secular evolution of compact star-planet systems.

A more thorough description of the different interactions regimes can be found in [66]. We refer the interested reader to this review and the references therein. In all cases, though, two Alfvén wings always form in the $(\mathbf{B}_w, \mathbf{v}^w - \mathbf{v}^{\text{kep}})$ plane. Depending on the Alfvénic Mach numbers (Eqs. (10)-(12)), both wings can connect onto the host star, only one may do so while the other extends away toward the interplanetary medium, or both may head away from the host star (see Figure 7). As a result, the knowledge of the magnetic configuration between the host star and the orbital path of the planet is mandatory to assess star-planet magnetic interactions.

4.2. *Observable effects of magnetic interactions*

The search for star-planet magnetic interactions has been a continuous history of positive and negative detections. The first detection (yet still debated) of a signal that could be related to star-planet magnetic interactions was reported in the CaII K band of HD 179949 [80], following a theoretical argument for the existence of star-planet magnetic interaction [81]. They monitored at that time 5 promising star-planet systems, and detected a modulation associated with the hot Jupiter orbital period only for HD 179949. The other systems did not show any evidence of star-planet magnetic interactions at that time. Such signals have been observed since for different systems (see the review [82]) such as famous compact star-planet systems like 55 Cnc or HD 189733 [83]. The star-planet interactions tracers found in the stellar activity indicators have always been subject to a large variability, with very clear signals at some epochs, and no detection at others [25, 84]. We believe today that at least part of this hide & seek stems for the

intrinsic, complex and variable nature of star-planet magnetic interactions. Star-planet magnetic interactions are controlled by the large-scale magnetism of stars, that can be topologically complex [85, 86] and time-variable due to eruptive events (e.g. flares and coronal mass ejections, on a monthly timescale [87]) or magnetic cycles (on the yearly to decadal timescale). As a result, star-planet magnetic interactions likely vary in nature and strength along planetary orbits as well as on longer timescales. The effect of magnetic topology has been recently unveiled for the case of HD 189733 [88] and is illustrated in Figure 8. In this system, the structuring of the stellar corona was modelled based on the magnetic topology of the central star characterized thanks to Zeeman–Doppler Imaging [89]. A synthetic chromospheric signal was produced (see lower panel in Figure 8), and was shown to be modulated by both the stellar rotational phase and the planet orbital phase. As a consequence, given the scarcity of past observational campaigns, the detection of a signal from available observation would be statistically likely only about 15% of the time. Such statistics explain at least part of the past successful and failed attempts for their detection in this system, and warrant much denser observational programs for their firm detection.

Historically, tracers of star-planet magnetic interaction have also been searched in radio. Indeed, compact star-planet systems look alike planet-satellite systems in our solar-system. The interaction of Io in the magnetosphere of Jupiter is known to lead to cyclotron-maser radio emissions near the poles of Jupiter [61]. At the same location, strikingly clear UV spots are present [90, 91], tracing the footprints of the magnetic interaction of Jupiter with Ganymede, Io, and Europa. Until recently, no clear radio detection of star-planet magnetic interactions have been successfully obtained [92]. In 2019-2020, two new observations hinted toward these long-awaited radio emissions. The first one was a cautious suspicion of a radio emission in the τ Boo system [93]. The second one was the detection of coherent radio emission from the red dwarf GJ 1151 [94]. The latter is an indirect detection, in the sense that the observed stellar radio emission is peculiarly intense compared to what is expected from such a slowly-rotating star. The authors showed that the observed emission could be compatible with star-planet magnetic interaction with an Earth-like planet on a 1 to 5 days orbit, but we have not detected this planet so far [95]. A firm detection of this hypothetical planet through transits or radial velocity would help strengthen our confidence in this detection scenario today. The detection of star-planet interactions through radio maser emissions is quickly growing with ambitious and dedicated observational program with instruments like NenuFAR [96].

Finally, the magnetic torque (Eq. (15)) can also lead to the migration of hot magnetized planets. The systematic comparison of tidal and magnetic torques [97] leads to the conclusion that magnetic torque can dominate the migration path for low-mass planets around low mass stars, whereas tides tend to dominate the migration of more massive close-in planets. These conclusions have further been supported using secular evolution models as well [55]. Therefore, the architecture of star-planet systems is also likely influenced by magnetic interactions.

5. Conclusions and perspectives

In this review I have introduced the physical concepts behind the three main star-planet interaction processes that occur in compact star-planet systems: high atmosphere irradiation and atmospheric escape, gravitational interaction in the form of tides, and magnetic interaction. For each process, I have reviewed simple approaches and scaling-laws describing them. I have also highlighted the key observational results which could originate from these interactions. Nevertheless, we still need to improve our physical understanding of these interactions to leverage the maximum information from the observational data we have at hand. For instance, the mere observation of a planet with a decaying orbit ([43], see § 3.2) provides a fantastic test bed for tidal
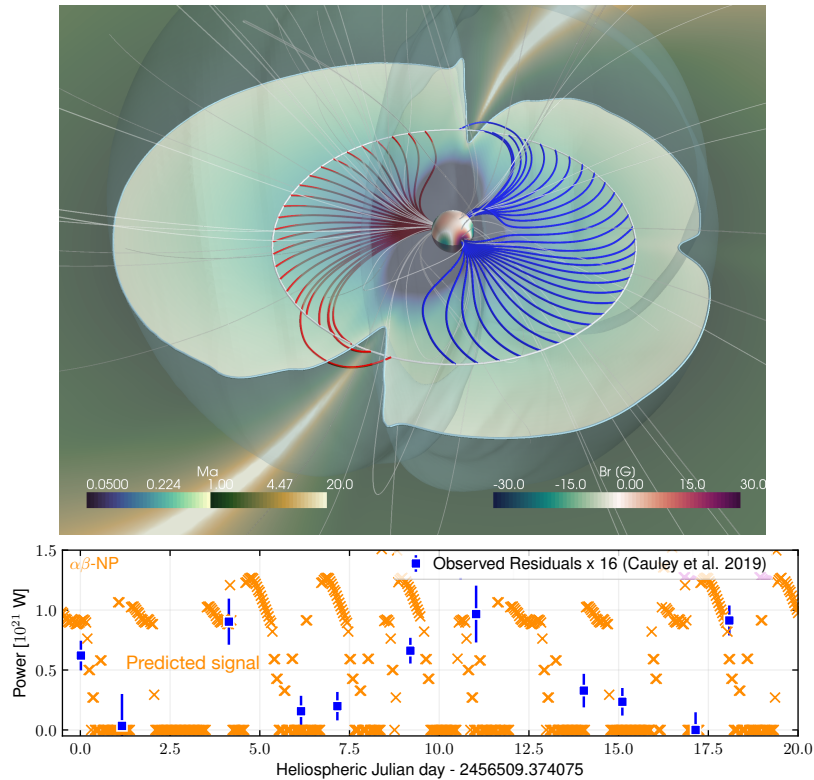
Figure 8. Predicted star-planet interaction pattern for HD 189733b [88] and detected signal [83]. In the top panel, the coronal structure is predicted from a stellar wind model leveraging the magnetic topology of HD 189733 observed in August 2013 [89]. The Alfvénic Mach number (Eq. (12)) is shown on the orbital plane with bright blueish colors ($M_a < 1$) and bright yellowish colors ($M_a > 1$). The Alfvén 3D surface is shown by the transparent blue surface, and the magnetic field lines by the gray tubes. The magnetic connectivity path is shown by the red and blue tubes. In this situation, one wing connects back to the star for half of the orbit, and the other wing ensures the connection for the other half of the orbit. In the bottom panel, a synthetic emission pattern is predicted based on the magnetic connectivity path above and on the orbital phase (orange crosses). The observational signal is shown by the blue squares [83]. This study demonstrates the need for much denser observational campaigns to clearly associate the detected signal with star-planet magnetic interactions. For more details, see [88].

and magnetic interaction theories, and for their use to characterize the internal properties of interacting star and planets.

Multiple groups have recently claimed to detect the long awaited tracers of star-planet magnetic interactions (see § 4.2). Still, the power predicted by models of magnetic interaction depends on ill-characterized parameters in compact star-planet systems (see § 4.1). This makes the estimates of the magnitude of these interactions imprecise, i.e. within at least an order of magnitude [98]. We need to go beyond this limitation and develop more precise models of star-planet interaction around cool stars. The main unknown today is how the energy carried in Alfvén wings is deposited in the stellar environment. Incoming Alfvén waves encounter a corona, eventually a

transition region, and some of them can permeate into the chromosphere and maybe the photosphere. It is challenging, yet feasible to model this sequence from ab-initio principles (see e.g. [99] for a step in this direction). In addition, the temporal phasing of star-planet magnetic interactions can be predicted based on the large-scale, 3D topology of distant stars [88]. The combination of both may allow the firm detection and characterization of star-planet magnetic interaction in a near future.

Finally, the joint study of star-planet magnetic interaction and atmospheric escape processes is needed today. These processes can be complex and depend on the type of exoplanet considered and its distance to its host star (see § 2.1 and [12]). Hydrodynamic and magneto-hydrodynamic models have been refined over the past five years to include at the same time the magnetic interaction itself [18, 100] and the self-consistent excitation of a hydrodynamic planetary wind embedding both neutral and ionized species [20, 21]. The development of these models will greatly help to interpret the wealth of multi-wavelength observational data that the various ground-based and space telescopes will provide to the exoplanet community in the coming decade.

Conflicts of interest

The authors have no conflict of interest to declare.

Acknowledgements

References

[1]   M. Mayor, D. Queloz, "A Jupiter-mass companion to a solar-type star", *Nature* **378** (1995), no. 6, p. 355-359.

[2]   K. Biazzo, V. Bozza, L. Mancini, A. Sozzetti, "The Demographics of Close-In Planets", in *Demographics of Exoplanetary Systems: Lecture Notes of the 3rd Advanced School on Exoplanetary Science*, Astrophysics and Space Science Library, vol. 466, Springer, 2022, p. 143-234.

[3]   C. Moutou, J.-F. Donati, F. Debras, "Les exoplanètes et leurs étoiles vues par SPIRou: vélocimétrie de précision dans l'infrarouge proche et spectropolarimétrie", *C. R. Phys.* **24** (2023), no. S2, Online first.

[4]   R. Galicher, J. Mazoyer, "Imager des exoplanètes grâce aux instruments coronographiques", *C. R. Phys.* **24** (2023), no. S2, Online first.

[5]   B. J. Fulton, E. A. Petigura, A. W. Howard *et al.*, "The California-*Kepler* Survey. III. A Gap in the Radius Distribution of Small Planets", *Astron. J.* **154** (2017), no. 3, article no. 109.

[6]   A. McQuillan, T. Mazeh, S. Aigrain, "Stellar Rotation Periods of the Kepler Objects of Interest: A Dearth of Close-in Planets around Fast Rotators", *Astrophys. J. Lett.* **775** (2013), no. 1, article no. L11.

[7]   R. K. Kopparapu, R. Ramirez, J. F. Kasting *et al.*, "Habitable zones around main-sequence stars: New estimates", *Astrophys. J.* **765** (2013), no. 2, article no. 131.

[8]   A. Lecavelier des Etangs, "A diagram to determine the evaporation status of extrasolar planets", *Astron. Astrophys.* **461** (2007), no. 3, p. 1185-1193.

[9]   B. J. Fulton, E. A. Petigura, "The California-*Kepler* Survey. VII. Precise Planet Radii Leveraging Gaia DR2 Reveal the Stellar Mass Dependence of the Planet Radius Gap", *Astron. J.* **156** (2018), no. 6, article no. 264.

[10] E. Chassefière, F. Leblanc, "Mars atmospheric escape and evolution; interaction with the solar wind", *Planet. Space Sci.* **52** (2004), no. 11, p. 1039-1058.

[11] H. Lammer, J. F. Kasting, E. Chassefière *et al.*, "Atmospheric escape and evolution of terrestrial planets and satellites", *Space Sci. Rev.* **139** (2008), no. 1-4, p. 399-436.

[12] G. Gronoff, P. Arras, S. Baraka *et al.*, "Atmospheric Escape Processes and Planetary Atmospheric Evolution", *J. Geophys. Res. Sp. Phys.* **125** (2020), no. 8, article no. e2019JA027639.

[13] E. N. Parker, "Dynamics of the Interplanetary Gas and Magnetic Fields", *Astrophys. J.* **128** (1958), no. 1905, p. 664.

[14] A. García Muñoz, "Physical and chemical aeronomy of HD 209458b", *Planet. Space Sci.* **55** (2007), no. 10, p. 1426-1455.

[15] R. E. Johnson, A. N. Volkov, J. T. Erwin, "Molecular-kinetic simulations of escape from the ex-planet and exoplanets: Criterion for transonic flow", *Astrophys. J. Lett.* **768** (2013), no. 1, article no. L4.

[16] N. V. Erkaev, H. Lammer, P. Odert *et al.*, "EUV-driven mass-loss of protoplanetary cores with hydrogen-dominated atmospheres: The influences of ionization and orbital distance", *Mon. Not. R. Astron. Soc.* **460** (2016), no. 2, p. 1300-1309.

[17] R. A. Murray-Clay, E. I. Chiang, N. Murray, "Atmospheric escape from hot Jupiters", *Astrophys. J.* **693** (2009), no. 1, p. 23-42.

[18] T. Matsakos, A. Uribe, A. Königl, "Classification of magnetized star-planet interactions: bow shocks, tails, and inspiraling flows", *Astron. Astrophys.* **578** (2015), article no. A6.

[19] C. V. D'Angelo, A. A. Vidotto *et al.*, "GJ 436b and the stellar wind interaction: simulations constraints using Ly-alpha and Halpha transits", http://arxiv.org/abs/2012.05128, 2020.

[20] M. L. Khodachenko, I. F. Shaikhislamov, H. Lammer *et al.*, "The impact of intrinsic magnetic field on the absorption signatures of elements probing the upper atmosphere of HD209458b", *Mon. Not. R. Astron. Soc.* **507** (2021), no. 3, p. 3626-3637.

[21] L. Wang, F. Dai, "Metastable Helium Absorptions with 3D Hydrodynamics and Self-consistent Photochemistry. I. WASP-69b, Dimensionality, X-Ray and UV Flux Level, Spectral Types, and Flares", *Astrophys. J.* **914** (2021), no. 2, article no. 98.

[22] L. N. R. do Amaral, R. Barnes, A. Segura, R. Luger, "The Contribution of M-dwarf Flares to the Thermal Escape of Potentially Habitable Planet Atmospheres", *Astrophys. J.* **928** (2022), no. 1, article no. 12.

[23] A. Vidal-Madjar, A. Lecavelier des Etangs, J. M. Désert *et al.*, "An extended upper atmosphere around the extrasolar planet HD209458b", *Nature* **422** (2003), no. 6928, p. 143-146.

[24] V. Bourrier, A. L. des Etangs, "Characterizing Evaporating Atmospheres of Exoplanets", in *Handbook of Exoplanets*, Springer, 2018, p. 1509-1526.

[25] E. L. Shkolnik, D. A. Bohlender, G. A. H. Walker, A. Collier Cameron, "The On/Off Nature of Star-Planet Interactions", *Astrophys. J.* **676** (2008), no. 1, p. 628-638.

[26] I. Pillitteri, A. Maggio, G. Micela *et al.*, "FUV variability of HD 189733. Is the star accreting material from its hot Jupiter?", *Astrophys. J.* **805** (2015), no. 1, article no. 52.

[27] L. Fossati, T. R. Ayres, C. A. Haswell *et al.*, "Absorbing Gas around the WASP-12 Planetary System", *Astrophys. J. Lett.* **766** (2013), no. 2, article no. L20.

[28] L. Fossati, T. Koskinen, K. France *et al.*, "Suppressed Far-UV Stellar Activity and Low Planetary Mass Loss in the WASP-18 System", *Astron. J.* **155** (2018), no. 3, article no. 113.

[29] J. E. Owen, D. Lai, "Photoevaporation and high-eccentricity migration created the sub-Jovian desert", *Mon. Not. R. Astron. Soc.* **479** (2018), no. 4, p. 5012-5021.

[30] J. E. Owen, Y. Wu, "The Evaporation Valley in the Kepler Planets", *Astrophys. J.* **847** (2017), no. 1, article no. 29.

[31] D. Kubyshkina, M. Lendl, L. Fossati *et al.*, "Young planets under extreme UV irradiation", *Astron. Astrophys.* **612** (2018), article no. A25.

[32] D. Kubyshkina, L. Fossati, N. V. Erkaev *et al.*, "Grid of upper atmosphere models for 1–40 Mearth planets: application to CoRoT-7 b and HD 219134 b,c", *Astron. Astrophys.* **619** (2018), article no. A151.

[33] G. I. Ogilvie, "Tidal dissipation in stars and giant planets", *Annu. Rev. Astron. Astrophys.* **52** (2014), p. 171-210.

[34] S. Mathis, "Tidal Star-Planet Interactions: A Stellar and Planetary Perspective", in *Handbook of Exoplanets* (H. J. Deeg, J. A. Belmonte, eds.), Springer, 2018, p. 1801-1831.

[35] J.-P. Zahn, "Les marées dans une étoile double serrée (suite)", *Ann. d'Astrophysique* **29** (1966), p. 489-506.

[36] J. G. Williams, D. H. Boggs, "Secular tidal changes in lunar orbit and Earth rotation", *Celest. Mech. Dyn. Astron.* **126** (2016), no. 1-3, p. 89-129.

[37] W. M. Kaula, "Tidal Dissipation by Solid Friction and the Resulting Orbital Evolution", *Rev. Geophys.* **2** (1964), no. 4, p. 661-685.

[38] G. I. Ogilvie, D. N. C. Lin, "Tidal Dissipation in Rotating Solar-Type Stars", *Astrophys. J.* **661** (2007), no. 2, p. 1180-1191.

[39] V. Lainey, R. A. Jacobson, R. Tajeddine *et al.*, "New constraints on Saturn's interior from Cassini astrometric data", *Icarus* **281** (2017), p. 286-296.

[40] F. Remus, S. Mathis, J.-P. Zahn, "The equilibrium tide in stars and giant planets. I. The coplanar case", *Astron. Astrophys.* **544** (2012), article no. 132.

[41] A. F. Lanza, "Orbital period modulation in hot Jupiter systems", *Mon. Not. R. Astron. Soc.* **497** (2020), no. 3, p. 3911-3924.

[42] M. Efroimsky, V. V. Makarov, "Tidal Quality of the Hot Jupiter WASP-12b", *Universe* **8** (2022), no. 4, article no. 211.

[43] I. Wong, A. Shporer, S. Vissapragada *et al.*, "TESS Revisits WASP-12: Updated Orbital Decay Rate and Constraints on Atmospheric Variability", *Astron. J.* **163** (2022), no. 4, article no. 175.

[44] K. C. Patra, J. N. Winn, M. J. Holman *et al.*, "The Apparently Decaying Orbit of WASP-12b", *Astron. J.* **154** (2017), no. 1, article no. 4.

[45] S. W. Yee, J. N. Winn, H. A. Knutson *et al.*, "The Orbit of WASP-12b Is Decaying", *Astrophys. J. Lett.* **888** (2020), no. 1, article no. L5.

[46] J. D. Turner, A. Ridden-Harper, R. Jayawardhana, "Decaying Orbit of the Hot Jupiter WASP-12b: Confirmation with TESS Observations", *Astron. J.* **161** (2021), no. 2, article no. 72.

[47] B. M. S. Hansen, "Calibration of Equilibrium Tide Theory for Extrasolar Planet Systems. II", *Astrophys. J.* **757** (2012), no. 1, p. 6.

[48] A. S. Bonomo, S. Desidera, S. Benatti *et al.*, "The GAPS Programme with HARPS-N at TNG", *Astron. Astrophys.* **602** (2017), article no. A107 (16 pages).

[49] A. C. Cameron, M. Jardine, "Hierarchical Bayesian calibration of tidal orbit decay rates among hot Jupiters", *Mon. Not. R. Astron. Soc.* **476** (2018), no. 2, p. 2542-2555, https://arxiv.org/abs/1801.10561.

[50] S. Mathis, "Variation of tidal dissipation in the convective envelope of low-mass stars along their evolution", *Astron. Astrophys.* **580** (2015), article no. L3.

[51] F. Pont, "Empirical evidence for tidal evolution in transiting planetary systems", *Mon. Not. R. Astron. Soc.* **396** (2009), no. 3, p. 1789-1796.

[52] Y. S. Messias, L. L. A. de Oliveira, R. L. Gomes *et al.*, "A dearth of close-in planets around rapidly rotating stars or a dearth of data?", http://arxiv.org/abs/2205.04893, 2022.

[53] E. Bolmont, S. N. Raymond, J. Leconte, S. P. Matt, "Effect of the stellar spin history on the tidal evolution of close-in planets", *Astron. Astrophys.* **544** (2012), article no. A124.

[54] M. M. Zhang, K. Penev, "Stars get dizzy after lunch", *Astrophys. J.* **787** (2014), no. 2, article no. 131.

[55] J. Ahuir, A. Strugarek, A.-S. Brun, S. Mathis, "Magnetic and tidal migration of close-in planets", *Astron. Astrophys.* **650** (2021), article no. A126.

[56] C. Mordasini, "Planetary population synthesis", in *Handbook of Exoplanets*, Springer, 2018, p. 2425-2474.

[57] F. Gallet, "TATOO: Tidal-chronology standalone tool to estimate the age of massive close-in planetary systems", *Astron. Astrophys.* **641** (2020), article no. A38.

[58] D. Verscharen, K. G. Klein, B. A. Maruca, "The multi-scale nature of the solar wind", *Living Rev. Sol. Phys.* **16** (2019), no. 1, p. 5.

[59] A. A. Vidotto, "The evolution of the solar wind", *Living Rev. Sol. Phys.* **18** (2021), no. 1, p. 3.

[60] A. Strugarek, "Physics of star-planet magnetic interactions", http://arxiv.org/abs/2104.05968, to appear in *Proceedings of the Evry Schatzman School 2019 "Interactions star-planet"*, 2021.

[61] P. Zarka, "Plasma interactions of exoplanets with their parent star and associated radio emissions", *Planet. Space Sci.* **55** (2007), no. 5, p. 598-617.

[62] E. J. Weber, L. J. Davis, "The Angular Momentum of the Solar Wind", *Astrophys. J., Suppl. Ser.* **148** (1967), p. 217-227.

[63] J. C. Kasper, C. H. K. Chen, Universite De Paris, J. Janssen, "*Parker Solar Probe* enters the magnetically-dominated solar corona", *Phys. Rev. Lett.* **127** (2021), no. 25, article no. 255101.

[64] P. Zarka, R. A. Treumann, B. P. Ryabov, V. B. Ryabov, "Magnetically-Driven Planetary Radio Emissions and Application to Extrasolar Planets", *Astrophys. Space Sci.* **277** (2001), no. 1, p. 293-300.

[65] F. M. Neubauer, "The sub-Alfvénic interaction of the Galilean satellites with the Jovian magnetosphere", *J. Geophys. Res. Planets* **103** (1998), no. E9, p. 19843-19866.

[66] A. Strugarek, "Models of star-planet magnetic interaction", in *Handbook of Exoplanets*, Springer, 2018, p. 1833-1855.

[67] P. Goldreich, D. Lynden-Bell, "Io, a jovian unipolar inductor", *Astrophys. J.* **156** (1969), p. 59-78.

[68] J. Saur, "A model of Io's local electric field for a combined Alfvénic and unipolar inductor far-field coupling", *J. Geophys. Res. Sp. Phys.* **109** (2004), no. A1, article no. A01210.

[69] R. O. Laine, D. N. C. Lin, "Interaction of Close-in Planets with the Magnetosphere of Their Host Stars. II. Super-Earths as Unipolar Inductors and Their Orbital Evolution", *Astrophys. J.* **745** (2012), no. 1, article no. 2.

[70] D. Lai, "DC circuit powered by orbital motion: Magnetic interactions in compact object binaries and exoplanetary systems", *Astrophys. J. Lett.* **757** (2012), no. 1, p. L3.

[71] A. F. Lanza, "Star-planet magnetic interaction and evaporation of planetary atmospheres", *Astron. Astrophys.* **557** (2013), article no. A31.

[72] F. M. Neubauer, "Nonlinear standing Alfvén wave current system at Io: Theory", *J. Geophys. Res. Sp. Phys.* **85** (1980), no. A3, p. 1171-1178.

[73] A. Strugarek, A.-S. Brun, S. P. Matt, V. Réville, "Magnetic games between a planet and its host star: the key role of topology", *Astrophys. J.* **815** (2015), no. 2, article no. 111.

[74] J. Saur, T. Grambusch, S. Duling, F. M. Neubauer, S. Simon, "Magnetic energy fluxes in sub-Alfvénic planet star and moon planet interactions", *Astron. Astrophys.* **552** (2013), article no. A119.

[75] A. Strugarek, "Assessing magnetic torques and energy fluxes in close-in star–planet systems", *Astrophys. J.* **833** (2016), no. 2, article no. 140.

[76] A. Strugarek, "Magnetic inclination effects in star-planet magnetic interactions", *EWASS Spec. Sess. 4 Star-planet Interact.* **4** (2017), p. 1-4.

[77] M. G. Kivelson, F. Bagenal, W. S. Kurth *et al.*, "Magnetospheric interactions with satellites", in *Jupiter. The planet, satellites and magnetosphere* (F. Bagenal, T. E. Dowling, W. B. McKinnon, eds.), Cambridge Planetary Science, vol. 1, Cambridge University Press, 2004, p. 513-536.

[78] C. P. Johnstone, M. L. Khodachenko, T. Lüftinger *et al.*, "Extreme hydrodynamic losses of Earth-like atmospheres in the habitable zones of very active stars", *Astron. Astrophys.* **624** (2019), article no. L10.

[79] A. Strugarek, A.-S. Brun, S. P. Matt, V. Réville, "On the diversity of magnetic interactions in close-in star–planet systems", *Astrophys. J.* **795** (2014), no. 1, article no. 86.

[80] E. L. Shkolnik, G. A. H. Walker, D. A. Bohlender, "Evidence for Planet-induced Chromospheric Activity on HD 179949", *Astrophys. J.* **597** (2003), no. 2, p. 1092-1096.

[81] M. Cuntz, S. H. Saar, Z. E. Musielak, "On Stellar Activity Enhancement Due to Interactions with Extrasolar Giant Planets", *Astrophys. J.* **533** (2000), no. 2, p. L151-L154.

[82] E. L. Shkolnik, J. Llama, "Signatures of Star-Planet Interactions", in *Handbook of Exoplanets*, Springer, 2017, p. 1-17.

[83] P. W. Cauley, E. L. Shkolnik, J. Llama, A. F. Lanza, "Magnetic field strengths of hot Jupiters from signals of star–planet interactions", *Nat. Astron.* **3** (2019), no. 12, p. 1128-1134.

[84] P. W. Cauley, E. L. Shkolnik, J. Llama *et al.*, "Evidence of Magnetic Star-Planet Interactions in the HD 189733 System from Orbitally Phased Ca II K Variations", *Astron. J.* **156** (2018), article no. 262.

[85] J.-F. Donati, J. D. Landstreet, "Magnetic Fields of Nondegenerate Stars", *Annu. Rev. Astron. Astrophys.* **47** (2009), no. 1, p. 333-370.

[86] V. See, M. Jardine, A. A. Vidotto *et al.*, "The energy budget of stellar magnetic fields", *Mon. Not. R. Astron. Soc.* **453** (2015), no. 4, p. 4301-4310.

[87] C. Fischer, J. Saur, "Time-variable Electromagnetic Star–Planet Interaction: The TRAPPIST-1 System as an Exemplary Case", *Astrophys. J.* **872** (2019), no. 1, article no. 113.

[88] A. Strugarek, R. Fares, V. Bourrier *et al.*, "MOVES – V. Modelling star–planet magnetic interactions of HD 189733", *Mon. Not. R. Astron. Soc.* **512** (2022), no. 3, p. 4556-4572.

[89] R. Fares, V. Bourrier, A. A. Vidotto *et al.*, "MOVES-I. The evolving magnetic field of the planet-hosting star HD189733", *Mon. Not. R. Astron. Soc.* **471** (2017), no. 1, p. 1246-1257.

[90] R. Prangé, D. Rego, D. Southwood *et al.*, "Rapid energy dissipation and variability of the Io-Jupiter electrodynamic circuit", *Nature* **379** (1996), no. 6, p. 323-325.

[91] J. T. Clarke, J. Ajello, G. E. Ballester *et al.*, "Ultraviolet emissions from the magnetic footprints of Io, Ganymede and Europa on Jupiter", *Nature* **415** (2002), no. 6875, p. 997-1000.

[92] P. Zarka, "Star-Planet Interactions in the Radio Domain: Prospect for Their Detection", in *Handbook of Exoplanets* (H. J. Deeg, J. A. Belmonte, eds.), Springer, 2018, p. 1775-1790.

[93] J. D. Turner, P. Zarka, J.-m. Grießmeier, "The search for radio emission from the exoplanetary systems 55 Cnc, Upsilon Andromedae, and Tau Boötis using LOFAR beam-formed observations", in *EPSC-DPS Jt. Meet. 2019*, vol. 13, EPSC, 2019, p. 4-5.

[94] H. K. Vedantham, J. R. Callingham, T. W. Shimwell *et al.*, "Coherent radio emission from a quiescent red dwarf indicative of star-planet interaction", *Nat. Astron.* (2020), p. 1-7, Online First.

[95] M. Perger, G. Anglada-Escudé, I. Ribas *et al.*, "Auto-correlation functions of astrophysical processes, and their relation to Gaussian processes. Application to radial velocities of different starspot configurations", *Astron. Astrophys.* **645** (2021), article no. A58.

[96] P. Zarka, L. Denis, M. Tagger *et al.*, "The low-frequency radio telescope NenuFAR", in *2018 2nd URSI Atlantic Radio Science Meeting (AT-RASC)*, IEEE, 2020, p. 2-5.

[97] A. Strugarek, E. Bolmont, S. Mathis *et al.*, "The Fate of Close-in Planets: Tidal or Magnetic Migration?", *Astrophys. J.* **847** (2017), no. 2, article no. L16.

[98] J.-M. Grießmeier, "Future Exoplanet Research: Radio Detection and Characterization", in *Handbook of Exoplanets* (H. J. Deeg, J. A. Belmonte, eds.), Springer, 2018, p. 3269-3283.

[99] J. Saur, S. Janser, A. Schreiner, G. Clark, B. H. Mauk *et al.*, "Wave-Particle Interaction of Alfvén Waves in Jupiter's Magnetosphere: Auroral and Magnetospheric Particle Acceleration", *J. Geophys. Res. Sp. Phys.* **123** (2018), no. 11, p. 9560-9573.

[100] S. Daley-Yates, I. R. Stevens, "Hot Jupiter accretion: 3D MHD simulations of star-planet-wind interaction", *Mon. Not. R. Astron. Soc.* **483** (2019), no. 2, p. 2600-2614.